



Evaporative cooling for polymer electrolyte fuel cells - An operando analysis at technical single cell level

Michael Striednig^a, Adrian Mularczyk^a, Wenmei Liu^a, Dirk Scheuble^a, Magali Cochet^a, Pierre Boillat^{a,b}, Thomas J. Schmidt^{a,c}, Felix N. Büchi^{a,*}

^a Electrochemistry Laboratory, Paul Scherrer Institut, Forschungsstrasse 111, CH-5232, Villigen PSI, Switzerland

^b Laboratory for Neutron Scattering and Imaging, Paul Scherrer Institut, Forschungsstrasse 111, CH-5232, Villigen PSI, Switzerland

^c Laboratory of Physical Chemistry, ETH Zürich, Vladimir-Prelog Weg 1-5/10, CH-8093, Zürich, Switzerland

HIGHLIGHTS

- Operando evaporative cooling analysis in a technical single cell.
- Evaporation is saturation limited at low and transport limited at high gas speed.
- Counter-flow is identified as optimal arrangement for evaporative cooling.
- Sufficient membrane humidification is provided by evaporative cooling.
- The performance is comparable to conventional cooling with humidified gases.

ARTICLE INFO

Keywords:

Polymer electrolyte fuel cell
PEFC
Evaporative cooling
Humidification
Operando experiment
Proof of concept

ABSTRACT

Evaporative cooling has the potential to reduce stack and system volume of polymer electrolyte fuel cells by up to 30% and to cut costs significantly by simplifying the multi-layered structure of bipolar plates and eliminating the need for external humidification.

This study provides an experimental proof of concept by analyzing the evaporation behavior, cooling power, internal humidification, electrochemical performance and operational stability of evaporative cooling under technical cell boundary conditions. Isothermal *in situ* as well as *operando* studies are carried out in an evaporatively cooled fuel cell (15 cm² active area, 80 °C, ambient pressure). Relative humidity boundary conditions imitate the inlet, center and outlet of a technical cell.

Main findings show that the evaporation rate is saturation limited at low gas velocities, whereas it is transport limited at higher gas speed. *Operando* measurements prove that evaporative cooling works at a technical cell level with multiple water supply lines. The entire waste heat is removed and sufficient membrane humidification is achieved when dry inlet gases are used. Furthermore, it is shown that optimal performance is achieved in a counter-flow arrangement. The observed electrochemical performance is comparable to conventional cooling with humidified gases at inlet, center and outlet of the cell.

1. Introduction

Polymer electrolyte fuel cells (PEFC) are recently gaining increased momentum in the automotive industry [1–4]. Especially in medium and heavy-duty transport applications, they are a viable alternative to internal combustion engines and battery powered drivetrains. PEFCs provide high volumetric and gravimetric power densities [5,6], system efficiencies above 60% [3], fast start-up times [2] and decent cold-start

capabilities [7]. Additionally, hydrogen as fuel enables high mileage and fast refueling [8,9].

However, to achieve a significant market share, several key performance indicators (e.g., dynamic behavior, efficiency, durability, power density and cold-start performance) need to be further improved [10]. Moreover, the continuous peak power of fuel cell systems in transport applications is still limited by the heat rejection to the environment and external humidification is required at elevated operating temperatures

* Corresponding author.

E-mail address: felix.buechi@psi.ch (F.N. Büchi).

<https://doi.org/10.1016/j.jpowsour.2022.232419>

Received 30 September 2022; Received in revised form 13 November 2022; Accepted 14 November 2022

Available online 30 November 2022

0378-7753/© 2022 The Authors. Published by Elsevier B.V. This is an open access article under the CC BY-NC-ND license (<http://creativecommons.org/licenses/by-nc-nd/4.0/>).

to ensure a sufficiently high ionic conductivity of the polymer electrolyte membrane [11]. Furthermore, fuel cell system costs need to be further reduced from 45 USD/kW_{net} (2015 status, projected for 500,000 units/year) [12] to 30 USD/kW_{net} or lower [10].

The conventional cooling system of polymer electrolyte fuel cells contributes significantly to stack and system mass, volume and cost. Evaporative cooling is a promising cooling and humidification concept for PEFCs. It shows the theoretical potential to reduce system mass and volume by up to 30% by eliminating the complex, multi-layered structure of bipolar plates as well as the need for external humidification [13, 14]. This, in turn, contributes to significant volume savings and cost reductions.

All evaporative cooling approaches have in common that a liquid (usually water) is fed to the fuel cell stack. It is either supplied to porous flow fields or bipolar plates [15–19], to additional devices or layers [20–23] or it is directly injected into the gas supply [24–27]. This, however, increases the complexity of bipolar plates or the cell and stack design in state-of-the-art evaporative cooling concepts. The stack is cooled by the latent heat, which is consumed during the phase change of water. Typically, the water vapor is removed with the exhaust gas.

The PSI evaporative cooling approach, presented by Cochet et al. [28], however, aims at reducing the complexity of bipolar plates. Therefore, a gas diffusion layer (GDL) with a mixed hydrophobic and hydrophilic pattern [29–33] is used. Liquid water is supplied with one or more water channels that are located in the anode flow field. The water is distributed within hydrophilic lines in the GDL, evaporates into the gas channel and thereby cools and humidifies the cell. Applying this concept does not require an additional layer and thus the complexity of the MEA is not increased.

Several numerical studies [13,34–39] presented in literature have analyzed evaporative cooling on material, cell, stack and system level. These studies coherently highlight the advantages and the high theoretical potentials of evaporative cooling for polymer electrolyte fuel cells. These include an improved humidification of the membrane, eliminating the need for an external humidifier, simplifying the structure of the bipolar plates and thus significant mass, volume, and cost saving potentials, respectively. A detailed literature study on numerical investigations of evaporative cooling can be found in our previous work [13,39].

Additionally, experimental studies of evaporative cooling have been conducted at material, cell, stack and system level and the phase change as well as the transport of water in GDLs has been studied extensively [40–46].

An evaporative cooling concept based on liquid water injection into the cathode air stream has been studied by Hwang and Kim [25] as well as by Choi et al. [24]. Both studies analyzed the humidification and cooling potential of liquid water injection by an external-mixing air-assist atomizer. They concluded the effectiveness of the technique for cooling and humidification purpose.

The PSI evaporative cooling approach has been analyzed so far on differential single cell level in our previous studies. Cochet et al. [28] used neutron radiography to visualize the water transport in an evaporatively cooled differential single cell with an active area of 4.4 cm². *In situ* experiments with a patterned GDL, fed by one water channel were conducted and the total heat flux was measured with heat flux sensors. The importance of the contact surface between water and gas flow and the impact of pressure, temperature, mass flow rates as well as the pattern of the hydrophilic lines, on the evaporation rate was analyzed using a simplistic 1-D model.

In a second study, Cochet et al. [47] measured *operando* performance data, accompanied by neutron imaging, under differential cell conditions. Only a slight performance decrease was reported compared to conventional cooling. Furthermore, positive effects of evaporative cooling on membrane humidification were observed.

Despite the number of numerical and experimental studies, there are still several challenges which have to be overcome. These include but

are not limited to: operational stability, inhomogeneous temperature and humidity distribution, freeze start capability, amount and quality of recovered water from the exhaust gas as well as the potential risk of enhanced cell degradation due to the increased relative humidity and temperature. Observed limitations of the evaporative cooling approach are discussed in detail in section 3.4 as well as in our previous work [13].

Additionally, literature has not provided insights into the evaporation behavior, cooling performance, internal humidification, electrochemical performance as well as operational stability of evaporative cooling under technical cell boundary conditions (i.e., non-differential operating conditions and thus changing relative humidity, reactant partial pressures, and temperature along the channel) yet.

Therefore, this work aims at providing a proof of concept for evaporative cooling with patterned GDLs under the boundary conditions of a technical single cell. In this study, we focus on the impact of the relative humidity changes along the channel, since the local water vapor partial pressure shows the strongest impact on evaporation and thus cooling performance. Temperature variations are not taken into account since a more homogeneous temperature distribution is expected with evaporative cooling (assuming an optimized GDL pattern). Furthermore, the small gradient in oxygen and hydrogen partial pressure along the channel has been neglected. The analyses are carried out at ambient pressure, due to the enhanced stability of evaporative cooling under these conditions. However, Cochet et al. [47] have shown that evaporative cooling also works at enhanced operating pressure but requires a more sophisticated control of the water pressure.

For this, a new 100 cm² fuel cell platform, which allows evaporative cooling under isothermal boundary conditions, was developed. New insights into the evaporation phenomena in the large cell are gained from *in situ* experiments with a 15 cm² active area and patterned GDL, fed by multiple water supply lines. The reduced GDL size allows for analyzing cooling power, internal humidification and electrochemical performance during *operando* fuel cell experiments at 80 °C at different simulated locations (inlet, center, outlet) in the large cell without complex local sensor instrumentation.

2. Experimental

In this study, *in situ* as well as *operando* experiments are carried out in a 100 cm² technical single cell (36 gas and 5 water channels) where the active area was restricted to about 15 cm². The water supply through 5 parallel water channels as well as the selected RH boundary conditions allow to extrapolate the results to a technical cell size, even though slight deviations are expected due to variations in temperature and oxygen partial pressure as well as due to enhanced edge effects with the smaller active area.

2.1. Experimental setup

2.1.1. Test station

All experiments presented in this study were performed on a custom-made test station. The cell temperature is controlled with a CC415 thermostat (Peter Huber Kältemaschinenbau AG, Germany) and a ZS3606NV electric load (Höcherl & Hackl GmbH, Germany) is used to record polarization curves. Gas flows are controlled by 5851S flow controllers (Brooks Instrument LLC, USA) and the supply lines are heated 5 °C above cell temperature with H3406 heating tubes (Horst GmbH, Germany) to avoid condensation. Relative humidity (RH) at the cell inlet is controlled with W-202A-220-K controlled evaporative mixers (CEM, Bronkhorst USA LLC, USA) and the dew point at anode and cathode outlet is measured with a HMT-317 dew point transmitter (Vaisala AG, Finland). Temperature as well as pressure is measured upstream and downstream of the cell with type K thermocouples (Bax Engineering GmbH, Germany) and PAA-33X absolute pressure transmitters (Keller AG, Switzerland). High frequency resistance (HFR) is measured with a model 3566 AC milliohm-meter (Tsuruga Electric

Corp., Japan) at 1 kHz. Deionized water for evaporative cooling is supplied with a model 110 syringe pump (kdScientific Inc, USA) and the water pressure is controlled with a riser column, which is also used to calculate the evaporation rate during *in situ* experiments by monitoring the level change over time. All sensors as well as the flow controllers have been calibrated prior to the series of experiments. The test station automation as well as data acquisition is based on NI SCXI-1000 hardware and LabVIEW™ 2018 (National Instruments Corp, USA).

2.1.2. Test cell

A custom-made test cell, which enables the supply of liquid water for evaporative cooling, has been designed for the *in situ* as well as the *operando* experiments. The setup is capable to hold several fuel cells (multi-cell or short stacks), however, for this study only one cell has been used. Furthermore, the design allows liquid cooling/heating to perform isothermal experiments. The cell is compressed with 8 screws (M8) which are tightened with a torque of 15 Nm (lubricated with PTFE spray) to provide a surface pressure of 2 MPa. Two identical graphite (BMA5 graphite composite, Eisenhuth GmbH & Co. KG, Germany) flow fields with 36 parallel gas channels ($0.8 \times 0.4 \text{ mm}^2$) and 5 water channels ($0.8 \times 1.5 \text{ mm}^2$) are used. For the *in situ* experiments, aluminum prototype flow fields with identical geometry are used. They provide higher mechanical stability, which is beneficial for repetitive cell assemblies, while their chemical stability is sufficiently high for experiments without electrochemical reactions. The gas supply manifold was designed with computational fluid dynamics (CFD) support in order to guarantee the same pressure drop for all channels. The membrane-electrode-assembly (MEA) is located in the center of the cell (see Fig. 1a, position ii) to ensure a developed gas flow as well as an equilibrium of gas temperature and cell temperature. Moreover, 0.8 mm thick polyolefin gaskets (Ice Cube, Freudenberg FST GmbH, Germany) are used to seal the cell.

2.1.3. Materials

Membrane-electrode-assemblies (MEA) with an active area of about 15 cm^2 ($65 \times 23.1 \text{ mm}^2$) were produced by hot-pressing cut-outs of Gore

Primea™ A510.1/M815.15/C510.4 (0.4 mg/cm^2 Pt loading at the cathode and 0.1 mg/cm^2 Pt loading at the anode, W.L. Gore and Associates, USA) catalyst coated membranes (CCM) with two $12.5 \mu\text{m}$ thick PEN sub-gaskets (Goodfellow Cambridge Ltd., UK) on a 3856CE hotpress (Carver Inc, USA) for 5 min at 140°C and 2 MPa. To align the different layers, hotmelt adhesive (Co-Polyamide Web, Abifor GmbH, Germany) was used outside the active area.

Fig. 1b shows the *operando* setup, whereas Fig. 1c indicates the *in situ* setup. At the cathode, Freudenberg H14C10 GDLs with MPL (6) were used. At the anode, different GDL combinations were used for *in situ* and *operando* experiments. It can be seen that both setups include a modified, patterned Toray TGP-H-060 GDL (3) which has been treated according to the procedure described below to produce a hydrophobic and hydrophilic pattern (approx. $500 \mu\text{m}$ hydrophilic line width and $950 \mu\text{m}$ hydrophobic spacing). The hydrophilic lines, are oriented perpendicular to the channels to distribute the water across the entire active area (see Fig. 1a). For both setups, a Freudenberg H14C10 GDL with MPL (2) was used towards the CCM to prevent the anode catalyst layer from flooding with liquid water from the hydrophilic lines.

In situ setup: For the *in situ* experiments, in addition to the patterned GDL, a Freudenberg H14C10 GDL with MPL with five $0.5 \times 20 \text{ mm}^2$ laser slits (4) above the water channels has been used to inhibit water breakthrough from the water channels into the gas channels. Additionally, the CCM of the cell has been replaced with a vapor tight polymer (1) (PEN, $25 \mu\text{m}$, Goodfellow Cambridge Ltd., UK) to limit the evaporation to one side of the cell (see Fig. 1c).

Operando setup: For the *operando* measurements, the H14C10 GDL with laser slits towards the gas channels was replaced by a Freudenberg H14i4 GDL without MPL (4) to increase the diffusive flux of water vapor through the GDL (see Fig. 1b).

The compression of the GDLs is controlled at 20% by introducing spacers made of PTFE coated glass fibers (Fiberflon GmbH, Germany). The uncompressed thickness of each GDL has been determined at 5 positions with a MarCator 1075R gauge (Mahr GmbH, Germany) and subsequently been averaged. The compressibility of the spacers was estimated with 7% at 2 MPa according to literature [48].

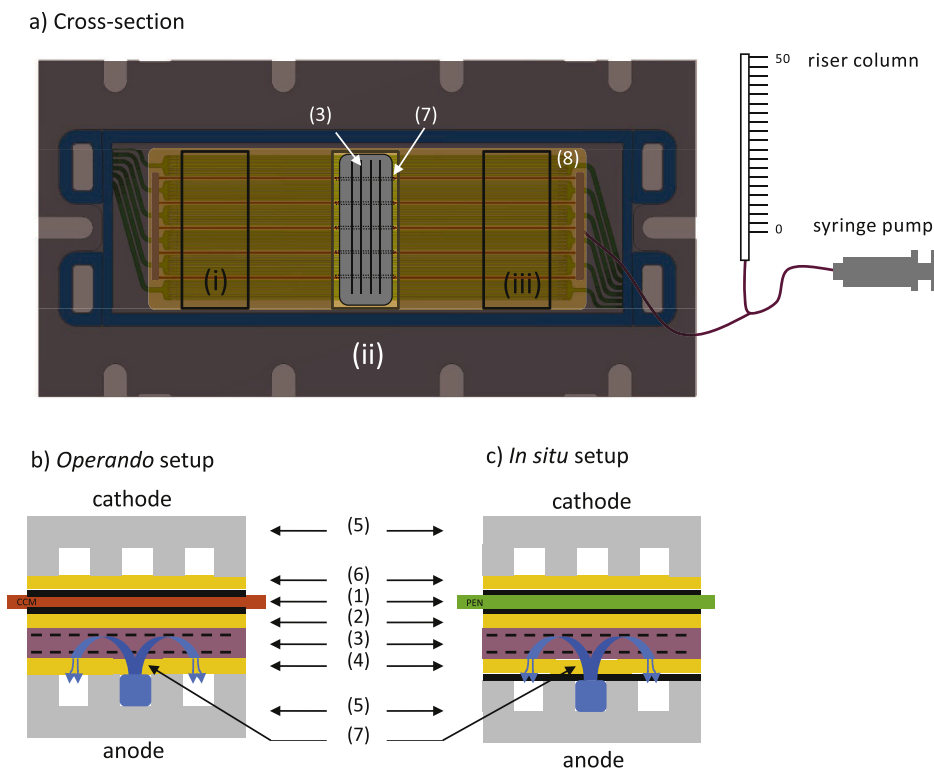


Fig. 1. a) flow field design with 36 gas channels (green), 5 water channels (orange), polyolefin gasket (blue) and indications for measurement positions (i-iii); b) cross-section of *operando* setup; c) cross-section of *in situ* setup (evaporation only). (1) CCM or PEN foil, (2) anode GDL with MPL, (3) patterned GDL, (4) hydrophobic water breakthrough inhibitor, (5) flow field, (6) cathode GDL, (7) laser slits, (8) hydrophobic spacer. (For interpretation of the references to color in this figure legend, the reader is referred to the Web version of this article).

Patterned GDL preparation: Commercial Toray paper (TGP-H-060, thickness of 190 μm , 78% porosity) was cleaned with ethanol, dried in a vacuum oven at 1 kPa before use and the dry weight was determined gravimetrically as m_0 . FEP dispersion (FEPD121, 55 wt% FEP, Dupont) was diluted with 0.95 parts of ultrapure water per dispersion to yield (70 ± 1.5) wt% of FEP coating. Dip coating method was used to deposit a thin layer of FEP to the carbon fiber surface for hydrophobicity treatment and to further modify the wettability by radiation grafting as reported in our previous work [29]. The GDL was immersed into the diluted FEP dispersion for 60 s, followed by the water evaporation procedure and a FEP sintering process described in the work mentioned above. Following that, the mass of the coated sample was taken as m_c . Coating load (C%) was calculated as follows:

$$C\% = \frac{m_c - m_0}{m_0} \quad (1)$$

The sample was then exposed to an electron beam in air (EBLab 200, Comet AG, Switzerland) using a 2 mm thick stainless steel mask patterned with 500 μm lines (electron-exposed region) and 950 μm spacing (electron-blocking region) to produce free radicals. The radiation was accelerated at 200 kV with a dose rate of 50 kGy. After bubbling with nitrogen for 1 h, the sample was grafted with pure N-vinyl-formamide (98%, Sigma-Aldrich) under nitrogen at 70 °C for 1 h. Only electron-exposed regions with free radicals were grafted to be hydrophilic during the process, while the blocked regions remain hydrophobic. After grafting, the GDL was cleaned with 300 mL of ethanol, isopropanol and water flowing through. After drying at 1 kPa and 60 °C, the weight of the samples (m_g) was measured.

2.2. Data analysis

The evaporation rate has been determined differently for the *in situ* and *operando* experiments. During the *in situ* experiments, the change in the water level in the riser column Δh was monitored over time t . With the diameter of the riser column d , the volumetric evaporation rate can be determined as follows:

$$\dot{V}_{\text{ev}} = \frac{d^2 \pi \Delta h}{4t} \quad (2)$$

The water level is determined with a precision ruler (0.5 mm scale) with a total uncertainty $u_{\Delta h}$ of ± 0.5 mm (± 0.25 mm at top and bottom measurement) and the uncertainty of the manual timing u_t is approximated with 0.1 s. Note: Whenever the term uncertainty is used, it indicates standard uncertainty according to reference [49]. The diameter of the tube was selected such that $\Delta h > 10$ mm and $t > 20$ s, to limit the uncertainty of the evaporation rate $u_{\dot{V}_{\text{ev}}}$. The uncertainty of the tube diameter d is neglected, since calibrated tubes and pipettes were used. Thus, the uncertainty of the evaporation rate $u_{\dot{V}_{\text{ev}}}$ can be calculated according to eq. (3) [49].

$$u_{\dot{V}_{\text{ev}}} = \frac{\partial \dot{V}_{\text{ev}}}{\partial \Delta h} u_{\Delta h} + \frac{\partial \dot{V}_{\text{ev}}}{\partial t} u_t \quad (3)$$

However, this method was not suitable for the *operando* measurements, since evaporation rates were less stable over time. Therefore, a method based on the measured dew point temperature at cathode $T_{\text{dp}}^{\text{ca}}$ and anode outlet $T_{\text{dp}}^{\text{an}}$ was applied. Assuming that the product water $\dot{n}_{\text{H}_2\text{O}}^{\text{rx}}$ exits the cell exclusively at the cathode and neglecting hydrogen as well as nitrogen crossover, the molar evaporation rates at anode $\dot{n}_{\text{ev}}^{\text{an}}$ and cathode $\dot{n}_{\text{ev}}^{\text{ca}}$ can be determined as follows:

$$\dot{n}_{\text{ev}}^{\text{an}} = \dot{n}_{\text{H}_2\text{O}}^{\text{an,out}} - \dot{n}_{\text{H}_2\text{O}}^{\text{an,in}} = \frac{\nu_{\text{H}_2\text{O}}^{\text{an,out}}}{1 - \nu_{\text{H}_2\text{O}}^{\text{an,out}}} \left(\dot{n}_{\text{H}_2}^{\text{an,in}} - \frac{jA_{\text{act}}}{2F} \right) - \dot{n}_{\text{H}_2\text{O}}^{\text{an,in}} \quad (4)$$

$$\dot{n}_{\text{ev}}^{\text{ca}} = \dot{n}_{\text{H}_2\text{O}}^{\text{ca,out}} - \dot{n}_{\text{H}_2\text{O}}^{\text{ca,in}} - \dot{n}_{\text{H}_2\text{O}}^{\text{rx}} = \frac{\nu_{\text{H}_2\text{O}}^{\text{ca,out}}}{1 - \nu_{\text{H}_2\text{O}}^{\text{ca,out}}} \left(\dot{n}_{\text{O}_2}^{\text{in}} + \dot{n}_{\text{N}_2}^{\text{in}} - \frac{jA_{\text{act}}}{4F} \right) - \dot{n}_{\text{H}_2\text{O}}^{\text{ca,in}} - \frac{jA_{\text{act}}}{2F} \quad (5)$$

with the molar flowrates of water vapor at anode inlet and outlet ($\dot{n}_{\text{H}_2\text{O}}^{\text{an,in}}$, $\dot{n}_{\text{H}_2\text{O}}^{\text{an,out}}$) respectively cathode inlet and outlet ($\dot{n}_{\text{H}_2\text{O}}^{\text{ca,in}}$, $\dot{n}_{\text{H}_2\text{O}}^{\text{ca,out}}$), the molar water production rate $\dot{n}_{\text{H}_2\text{O}}^{\text{rx}}$, molar fraction of water vapor at anode and cathode outlet ($\nu_{\text{H}_2\text{O}}^{\text{an,out}}$, $\nu_{\text{H}_2\text{O}}^{\text{ca,out}}$), the molar flowrates of hydrogen at anode inlet $\dot{n}_{\text{H}_2}^{\text{an,in}}$ and oxygen as well as nitrogen at cathode inlet ($\dot{n}_{\text{O}_2}^{\text{in}}$, $\dot{n}_{\text{N}_2}^{\text{in}}$), current density j , active Area A_{act} and Faraday constant F . The detailed derivation can be found in the supplementary information.

Note: Since liquid water is only introduced at the anode in the investigated concept, the cathode evaporation rate $\dot{n}_{\text{ev}}^{\text{ca}}$ is therefore a measure for the water transport through the MEA by diffusion and electro-osmotic drag.

The molar fraction of water vapor $\nu_{\text{H}_2\text{O}}$ at anode and cathode outlet have been calculated based on the measured dew point temperature T_{dp} and total pressure p_{tot} as follows (coefficients A, B and C are discussed in the supplementary information):

$$\nu_{\text{H}_2\text{O}} = \frac{p_{\text{H}_2\text{O}}}{p_{\text{tot}}} = \frac{10^{A - \frac{B}{C + T_{\text{dp}}}}}{p_{\text{tot}}} \quad (6)$$

Molar flow rates of hydrogen, oxygen and nitrogen are controlled by flow controllers whereas the molar flow rates of water vapor at cell inlet are controlled by the CEMs.

Since the uncertainty in dew point temperature $u_{T_{\text{dp}}}$ is expected to be dominant, the uncertainty of the evaporation rate $u_{\dot{n}_{\text{ev}}}$ is estimated as follows:

$$u_{\dot{n}_{\text{ev}}} \approx \frac{\partial \dot{n}_{\text{ev}}}{\partial T_{\text{dp}}} u_{T_{\text{dp}}} \quad (7)$$

The volumetric evaporation rate \dot{V}_{ev} can be calculated with the molar mass of water $M_{\text{H}_2\text{O}}$ and the density of liquid water at 25 °C, $\rho_{\text{H}_2\text{O}}$ as follows:

$$\dot{V}_{\text{ev}} = \frac{\dot{n}_{\text{ev}} M_{\text{H}_2\text{O}}}{\rho_{\text{H}_2\text{O}}} \quad (8)$$

During the measurement of polarization curves the above mentioned quantities as well as cell voltage and current density were averaged over 30 s after a holding period of 300 s.

The waste heat of the cell \dot{Q}_{wh} has been estimated as follows:

$$\dot{Q}_{\text{wh}} = (E_{\text{th}} - E_{\text{cell}}) \cdot J \quad (9)$$

with thermal voltage E_{th} , measured cell voltage E_{cell} and current J .

The thermal voltage is calculated according to equation (10). Due to the low impact in the relevant operating range (<100 °C), the temperature dependence of the thermal voltage is neglected.

$$E_{\text{th}} = - \frac{\Delta H^{\text{R}}(T)}{zF} \approx - \frac{\Delta H^{\text{R},0}}{zF} \approx 1.25 \text{ V} \quad (10)$$

With the temperature dependent enthalpy of reaction $\Delta H^{\text{R}}(T)$, number of transferred electrons z , Faraday constant F and standard enthalpy of reaction $\Delta H^{\text{R},0}$.

2.3. Experimental procedures

For the *in situ* evaporation analysis temperature, gas type as well as flowrate have been varied. Table 1 gives an overview of the investigated operating conditions.

For the *operando* analysis, measurements were conducted at ambient pressure and with isothermal boundary conditions at 80 °C cell temperature. In order to simulate a differential element at cell inlet, center

Table 1
In situ operating conditions.

Temperature	40, 60, 80, 90 °C
Gas Type	Nitrogen, Hydrogen
Pressure	Ambient Pressure
Volumetric gas flowrate	0.3 to 2 SCCM

and outlet (see Fig. 1a), a stoichiometric ratio of 10 was used at cathode and anode with a minimum flow of 0.3 SCCM. This is equivalent to a stoichiometric ratio of 1.5 if the entire active area of 100 cm² of the cell would have been used. Pure hydrogen is supplied at the anode and air at the cathode. Additionally, the relative humidity boundary conditions have been set to mimic the following three use cases:

- 1) Conventional cooling in a counter-flow arrangement with humidified gases
- 2) Evaporative cooling in a co-flow arrangement with dry gases
- 3) Evaporative cooling in a counter-flow arrangement with dry gases

Table 2 gives an overview of the RH boundary conditions for the respective test cases.

Conventional cooling counter-flow: External humidification is assumed at the cathode as is the recirculation of humid hydrogen at the anode. Therefore, a relative humidity boundary condition of 50% is set at anode and cathode inlet whereas full humidification (100% RH) is assumed at the respective outlet. In the center of the cell an intermediate relative humidity of 75% is estimated for hydrogen and air. The assumption of saturated outlets as well as a non-linear increase of the relative humidity along the channel is in line with simulation data provided by Grimm et al. [50].

Evaporative cooling co-flow: Both evaporative cooling arrangements assume the supply of dry gases at the cell inlet and a linear relative humidity increase along the channel (i.e., optimized GDL pattern, see section 3.4). In the co-flow arrangement, dry hydrogen (0% RH) and dry air (0% RH) are supplied at the same side of the cell, leading to a parallel increase in humidity along the cell. A relative humidity of 50% is assumed for hydrogen and air in the center of the cell whereas 90% RH is assumed at the cell outlet.

Evaporative cooling counter-flow: In the counter-flow arrangement, the dry gases are supplied at the opposite side of the cell. This yields a humidified cathode gas (90% RH) at the dry anode inlet (0% RH) and vice versa. At the center of the cell a relative humidity of 50% is assumed for hydrogen and air.

3. Results and discussion

3.1. Evaporation behavior and corresponding cooling power

First, the general water evaporation behavior from the hydrophilic lines in the patterned GDL, fed by multiple water channels, as function of dry gas speed, operating temperature and carrier gas is of interest, which also allows the determination of the achievable specific cooling power. This is straightforwardly assessed in a non-operated cell configuration to avoid interference with electrochemically produced water and transmembrane water transport due to electro-osmotic drag and diffusion.

Table 2
Relative humidity boundary conditions for three different configurations at three cell positions.

Configuration	Cell Inlet (i)		Cell Center (ii)		Cell Outlet (iii)	
	Anode RH	Cathode RH	Anode RH	Cathode RH	Anode RH	Cathode RH
Conventional Cooling: Counter-Flow (1)	50%	100%	75%	75%	100%	50%
Evaporative Cooling: Co-Flow (2)	0%	0%	50%	50%	90%	90%
Evaporative Cooling: Counter-Flow (3)	0%	90%	50%	50%	90%	0%

Gas velocity dependence of the evaporation rate: Fig. 2 shows the measured evaporation rates and the corresponding calculated cooling power densities (square markers) at 80 °C, ambient pressure and with dry nitrogen as a carrier gas. A linear increase is observed at lower gas speeds, whereas the gradient decreases with increasing gas speed and almost plateaus at high velocities. This effect is attributed to the change in the evaporation regime, or more precisely the mass transport regime of water vapor. At low gas speeds (blue area), the evaporation rate is only limited by the saturation of the carrier gas in the gas channels (blue line). Evaporation kinetics and diffusive transport of water vapor through the GDL and boundary layer in the gas channels are fast, compared to the convective gas flow. At higher gas speeds (red area), however, these transport phenomena become limiting and are therefore the determining step for the overall evaporation rate. Similar effects were observed in prior work in small imaging cells (active area: 0.1 cm²) [46] with non-modified GDLs and in differential cells with patterned GDLs with a single water supply line (active area: 4.4 cm²) [28]. More detailed interpretations of the occurring phenomena, supported by two-dimensional water vapor transport simulations, can be found in our previous work [46].

The data presented in Fig. 2 confirms that these effects also occur on the larger cell scale with multiple water supply lines. Furthermore, it can be seen that a linear correlation between evaporation rate and gas speed is only given up to 0.3 m/s at 80 °C. The corresponding calculated cooling power densities show that in the linear regime, the evaporation rate is too small to remove the estimated waste heat of the cell (dashed line) at a typical operation point of 1 A/cm² (and 0.6 V). Therefore, an increased temperature or an enhanced water vapor transfer through the membrane along the cell is required to remove sufficient heat.

Temperature dependence of the evaporation rate: It is important to understand the temperature dependence of the evaporation rate. Fig. 3 presents the impact of temperature (40–90 °C) on the evaporation

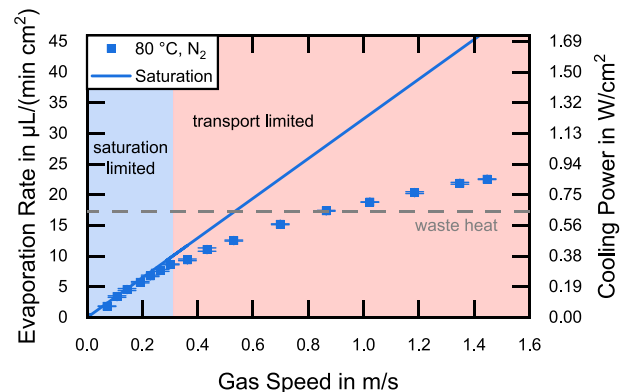


Fig. 2. Measured evaporation rates and calculated areal cooling power densities over gas speed (blue squares) as well as calculated saturation limited evaporation rate (blue line). *In situ* experiments at 80 °C, ambient pressure and dry nitrogen as carrier gas. Estimated waste heat at 1 A/cm² (assumed cell voltage: 0.6 V) shown as grey dashed line. Saturation limited region at low gas velocities (blue) and transport limited regime (red) at gas speeds above 0.3 m/s. (For interpretation of the references to color in this figure legend, the reader is referred to the Web version of this article).

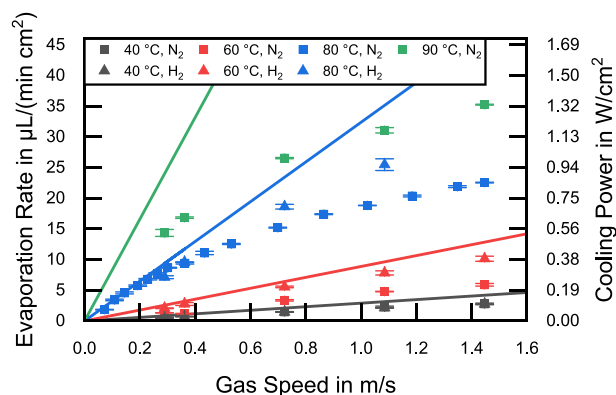


Fig. 3. *In situ* evaporation rates and calculated areal cooling power densities at ambient pressure and different operating temperatures between 40 and 90 °C. Nitrogen (square markers) or hydrogen (triangular markers) has been used as carrier gas. (For interpretation of the references to color in this figure legend, the reader is referred to the Web version of this article).

rate and cooling power. First, an over-proportional increase in evaporation rate with temperature is observed. This is mainly attributed to the non-linear nature of the saturation pressure which increases with temperature and thus allows a higher water vapor concentration and thus evaporation rate. Additionally, the diffusivity of water vapor in the carrier gas increases with higher temperature and thus allows a faster transport of water vapor through the GDL and the boundary layer in the gas channel. In our previous work [46], we have observed that the evaporation rate follows the saturation limitation to higher gas velocities at higher temperatures. This effect is less pronounced in Fig. 3 and the evaporation rates at 90 °C even show an exception to this behavior: The evaporation rate deviates earlier from the saturation limitation and is generally lower than expected. We hypothesize that this behavior is caused by a limited stability of the water supply due to an increased formation of vapor bubbles in the GDL and water supply channel at high temperatures and high evaporation rates. Furthermore, we hypothesize that a temperature gradient between the heated endplate and the actual evaporation zone is leading to a lower temperature at the water/gas interface and thus reduces the evaporation rate. With the highest heat fluxes, this influence is most noticeable at 90 °C.

Calculating the cooling power at 90 °C reveals that a waste heat of 1 W/cm² can be removed at gas speeds above 0.7 m/s. However, since 90 °C is considered the limit for continuous operation for state-of-the-art perfluorosulfonic-acid (PFSA) membranes and limitations regarding the operational stability are observed, it is important to investigate the impact of the carrier gas to further increase the evaporation rates at lower operating temperatures.

Carrier gas dependence of the evaporation rate: With hydrogen as carrier gas (Fig. 3, triangular markers), it is observed that the evaporation rates follow the saturation longer than with nitrogen, which is explained by the higher diffusivity of water vapor in hydrogen compared to nitrogen. Additionally, this leads to a higher level of the plateau at high gas velocities. At 80 °C, the max evaporation rate in hydrogen is about 30% higher than in nitrogen. Further, it can be seen that the corresponding cooling power exceeds 1 W/cm² considering only evaporation into the gas channels on one side of the cell. However, at 80 °C, this is achieved at gas speeds and thus stoichiometric ratios, which are considered too high for an efficient operation at system level. See our previous work [39]. Therefore, an increased water vapor transfer through the membrane is required along the gas channels to achieve sufficient cooling power at lower stoichiometric ratios. Furthermore, the results have to be substantiated during operation.

3.2. Fuel cell performance and humidification

In order to analyze the evaporation rates and cooling performance in a full cell, *operando* measurements were performed. Fig. 4 compares the performance of evaporative cooling in three different operating arrangements: 1) conventional operation counter-flow, 2) evaporative cooling co-flow and 3) evaporative cooling counter flow at a) cell inlet (anode inlet) b) center and c) cell outlet (anode outlet). The different positions and operating modes are emulated by choosing suitable RH boundary conditions for the reactant gases. The operating conditions are set for each test case according to Table 2.

The conventional cooling test case in counter-flow arrangement (black squares) serves as the base case. External humidification at the cathode and recirculation of humid hydrogen at the anode is assumed. Fig. 4 shows a slightly different performance for the base case (0.7–0.8 A/cm², ca. ±8% at 0.6 V) at the different cell positions. This effect is a bit smaller compared to literature values (<±15% reported in a modelling study by Gu et al. [51]). We attribute this to the neglected change in oxygen partial pressure that occurs along the channel in a technical cell. However, since this effect occurs for all presented concepts, the results still remain comparable. The generally lower performance compared to state-of-the-art materials and conditions is mainly explained by the ambient pressure operation. Furthermore, the HFR is similar at the three positions (80–90 mΩcm²). We attribute the comparably high HFR to the multi-layer GDL structure at the anode with increased contact resistances.

The fuel cell performance for the three operating modes shows the following characteristics at cell inlet, center and outlet:

Cell inlet: At the cell inlet (Fig. 4a) evaporative cooling in the counter-flow arrangement (blue triangles) performs similar to conventional, humidified operation (black squares). This is explained by the high saturation of the air at the cathode outlet, which is also reflected by a similar HFR. Evaporative cooling in the co-flow arrangement (red circles) shows a similar performance at lower current densities (<0.5 A/cm²). At higher current densities, however, the polarization curve shows a steeper gradient which is attributed to a significantly increased HFR at the dry cell inlet (both gases dry). Additionally, it can be observed that the HFR of the co-flow evaporative cooling arrangement increases with increasing current densities. RH measurements at the outlet (presented in the supplementary information) indicate that the anode is fully saturated over a wide range of current densities, whereas the cathode shows generally a lower humidity level and seems to dry out with higher flowrates at higher current which can explain the increase in HFR.

Cell center: At the center of the cell (Fig. 4b), a similar performance is observed when comparing the conventional cooling (black squares) with evaporative cooling in co-flow (red circles) and counter-flow arrangement (blue triangles). Even though, the HFR of both evaporative cooling concepts is slightly higher in comparison to conventional cooling, a slightly better performance is observed, which might be attributed to a higher oxygen partial pressure due to the slightly lower RH conditions.

Cell outlet: At the cell outlet (Fig. 4c), evaporative cooling in the counter-flow configuration (blue triangles) shows a similar or even slightly better performance than conventional cooling due to the high saturation of the anode outlet. Further, no significant difference in HFR is observed. At the cell outlet also evaporative cooling in the co-flow arrangement (red circles) shows a similar performance over a wide range of current densities and an even lower HFR. This is explained by the high humidification levels (90% RH) of hydrogen and air at anode and cathode outlet. However, at highest current densities the performance deviates and the HFR suddenly drops. This might indicate an unstable water supply and thus the presence of too much liquid water in the cell, which, in turn, leads to increased mass transport losses.

Based on the results presented in Fig. 4, we draw the conclusion that evaporative cooling works under technical cell conditions and it performs best in a counter-flow arrangement, since similar to conventional

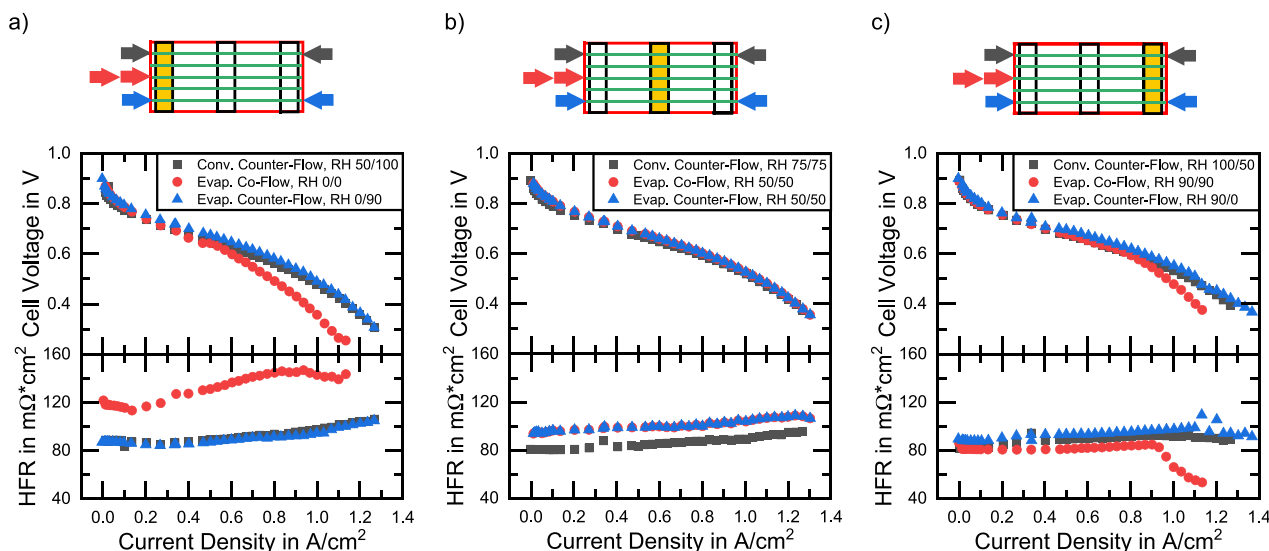


Fig. 4. Electrochemical performance with H_2 /air at $80\text{ }^\circ\text{C}$, ambient pressure and a stoichiometric ratio of 10 at cathode and anode at a) cell inlet, b) center and c) cell outlet. Colors indicate three different operating modes: conventional cooling counter-flow (black squares), evaporative cooling co-flow (red circles) and evaporative cooling counter-flow (blue triangles). RH indication: anode/cathode. (For interpretation of the references to color in this figure legend, the reader is referred to the Web version of this article).

cooling, too dry and too humid conditions are avoided.

3.3. Operando evaporative cooling performance

To gain further insights into the evaporation process in an operating cell, the corresponding evaporation rates have been determined under cell inlet, center and outlet conditions for the counter-flow arrangement. Evaporation rates and cooling performance have been calculated from the water injection rates at cell inlet and the dew point measurements at

cell outlet according to equations (4) and (5) given in the experimental section (see above).

Fig. 5 shows evaporation rates at cathode and anode as well as the concurring heat fluxes for evaporative cooling in the counter-flow arrangement. Again, the subfigures indicate the different positions at cell inlet (a,d), center (b,e) and outlet (c,f). The following evaporation characteristics were determined:

Cell inlet: At the cell inlet (Fig. 5a), it can be observed that the major share of evaporation happens at the anode (red squares). At the cathode

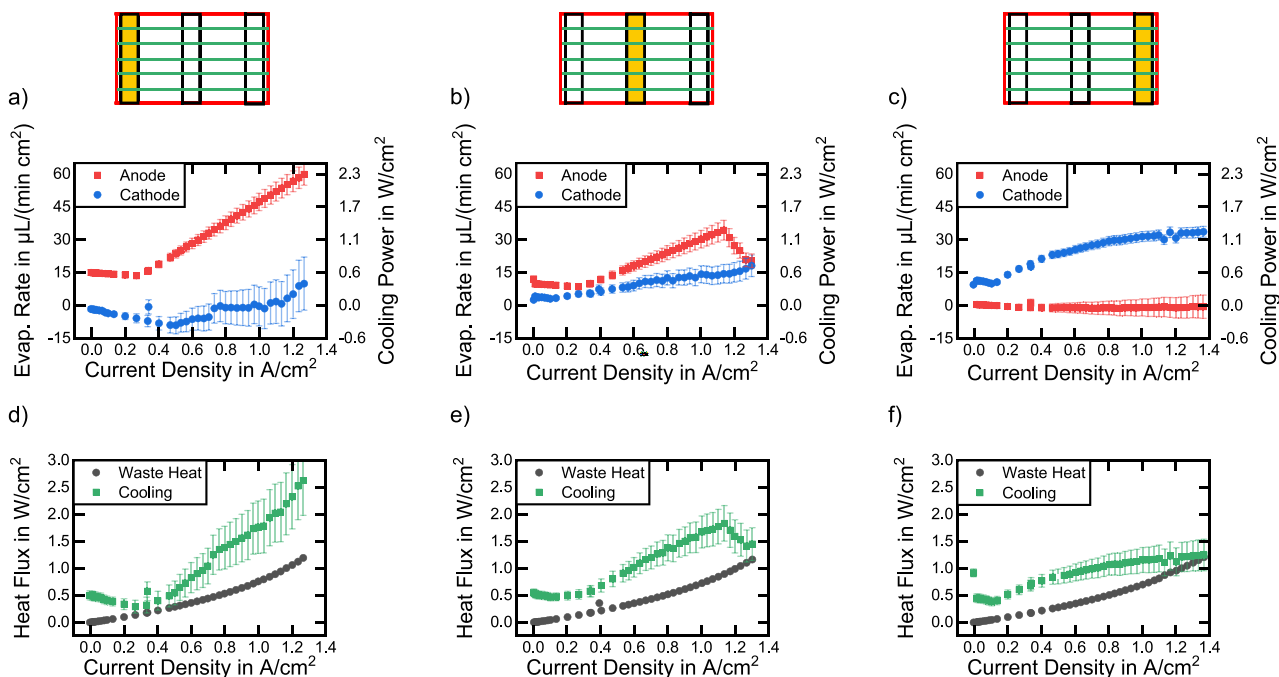


Fig. 5. Evaporation rates and areal cooling power density at a) cell inlet, b) center and c) outlet at the anode (red squares) and the cathode (blue circles). Subfigures d to f show the total cooling power density (cathode and anode combined, green squares) as well as the calculated waste heat of the cell ($(E_{th} - E_{cell}) \cdot j$, black circles) at inlet, center and outlet. Operating conditions: $80\text{ }^\circ\text{C}$, ambient pressure, H_2 /air, stoichiometric ratio 10 at cathode and anode and RH according to Table 2. (For interpretation of the references to color in this figure legend, the reader is referred to the Web version of this article).

(blue circles) no evaporation takes place except for a slight increase at highest current densities. This is obvious, since the anode inlet is dry (0% RH) and the counter-flow cathode is well-humidified (90% RH) in this case. Further, it can be seen that the evaporation at the anode is limited by the saturation of the gas stream which is indicated by the linear increase in evaporation rate with current density and thus with gas velocity due to the constant stoichiometry. RH measurements (presented in the supplementary information) show full saturation for the anode over the entire current density range.

Cell outlet: At the cell outlet (Fig. 5c), the behavior is opposite. The hydrogen at the anode is close to saturated (90% RH) whereas the air at the cathode is dry (0% RH). It can be seen that the evaporation exclusively takes place at the cathode (blue circles). However, compared to the cell inlet (Fig. 5a) the evaporation rate shows a logarithmic course with current density and gas velocity. This clearly indicates a transport limitation (see discussion of Fig. 2), since the water from the hydrophilic lines in the anode has to be transported through the CCM and then diffuse through the cathode gas diffusion layer to be removed with the cathode gas.

Cell center: In the center of the cell (Fig. 5b), evaporation takes place at anode (red squares) and cathode (blue circles) concurrently, though the evaporation at the anode is prevailing. It can be seen that at the anode the evaporation is still limited by saturation (linear course of evaporation rate with current density) whereas the evaporation towards the cathode is transport limited. However, the logarithmic behavior is less pronounced as compared to the cell outlet. At high current densities, the evaporation rate at the anode suddenly drops, which indicates an unstable operation of evaporative cooling. We hypothesize that the increased gas pressure (due to the increased pressure drop at high current densities) pushed liquid water out of the hydrophilic lines. Due to the stochastic morphology of the GDL, slight and random differences in water saturation can limit the stability of the water supply. This might explain why the effect only occurred in this measurement series. Nevertheless, it is worth mentioning that controlling the capillary pressure is key for a stable operation under evaporative cooling conditions.

Note: The constant evaporation rates at all positions at low current densities are given by the constant minimal gas flow rate of 0.3 SCCM.

Sub-figures d to f in Fig. 5 present the total evaporation rate expressed as heat flux (sum of cathode and anode evaporation rates, green squares) and the waste heat of the cell (black circles). It can be observed that the cooling power is highest at the inlet (above 2.5 W/cm²) due to the high, saturation-limited evaporation at the anode. Further, it can be seen that the cooling power is lowest at the cell outlet (ca. 1.25 W/cm²), which is explained by the prevailing lower, transport-limited evaporation at the cathode. However, it can be stated that the entire waste heat can be effectively removed by evaporative cooling at cell inlet, center and outlet.

3.4. Observed limitations of the evaporative cooling approach

Experimental results have shown that the high evaporation rates quickly saturate the gas channels, which will significantly lower the evaporation down the channel. This will in turn lead to a strong spatial gradient in cooling performance and thus in temperature. In order to mitigate this effect, the hydrophilic pattern has to be adapted along the channel (i.e., decreased spacing and/or increased width of the hydrophilic lines).

In addition, the experiments have unveiled the limited stability of the evaporative cooling approach. Breakthrough of liquid water into the gas channel requires only minor overpressure. This is critical at a technical cell level, since the gas pressure changes significantly along the channel. Thus, transient as well as pressurized operation is considered challenging for the patterned GDL approach for evaporative cooling. In this work a separate hydrophobic gas diffusion layer has been used as a mitigation measure. However, without further optimization, this comes

at the cost of an increased electrical contact resistance. To further improve the maturity of evaporative cooling and reduce the number of layers, this hydrophobic water breakthrough inhibitor shall be produced by chemical treatment in the future and be integrated directly into a 3-dimensional design of the GDL with patterned wettability. Additional improvements can be achieved by adapted control strategies (e.g., controlling the capillary pressure).

4. Conclusion

In this work, an experimental study of evaporative cooling for polymer electrolyte fuel cells using the patterned GDL concept has been performed. *In situ* and *operando* experiments were carried out at a technical cell level and evaporation rates, cooling power as well as electrochemical performance and internal humidification were evaluated.

In situ experiments with 15 cm² patterned GDLs, fed by five water channels, showed that two different evaporation regimes exist. At lower gas speed the evaporation rate is limited by the saturation of the gas stream, whereas it is limited by the diffusive transport of water vapor at higher velocities. This fact is relevant for future modelling work, since previous studies [13,36] assumed a linear correlation of evaporation rate and gas speed. The operating window for evaporative cooling that we proposed in our previous work, however, is not affected by this fact, since an operation at low pressure, high temperature and low to medium stoichiometry has been proposed [13,39].

Operando measurements have shown that the evaporative cooling concept works at a technical cell size with multiple water supplies. A satisfying membrane humidification is achieved even with dry inlet gases, and the optimal performance is obtained in a counter-flow arrangement. A comparable performance to conventional cooling and sufficient cooling power is achieved to reject the entire waste heat by evaporative cooling at cell inlet, center and outlet.

However, limitations regarding the stability of the liquid water supply were observed at high operating temperatures as well as high current densities and thus gas velocities. Further developments regarding optimized control strategies as well as improved GDL materials are required to ensure a stable operation.

Furthermore, the high evaporation rates lead to a fast saturation increase along the gas channels which would lead to uneven cooling and humidification for longer gas channels and thus to local temperature and current gradients. Adapting the pattern of the hydrophilic lines can help mitigating this effect. The experimental results presented in this paper as well as the modelling approaches presented in our prior work [13,39,46] can contribute significantly to the development of optimal structures.

In this study, the PSI evaporative cooling approach using water evaporation from patterned GDLs has been implemented for the first time at a technical cell size with multiple water supplies and experimental results have proven its viability as a combined cooling and humidification concept for PEFC, which would allow for a significant reduction of stack and system volume as well as mass and cost. Nevertheless, further improvements on the material level as well as adapted control strategies are required to increase the concept's technological maturity.

CRedit authorship contribution statement

Michael Striednig: Methodology, Conceptualization, Formal analysis, Visualization, Investigation, Writing – original draft. **Adrian Mularczyk:** Methodology, Writing – review & editing. **Wenmei Liu:** Resources, Writing – review & editing. **Dirk Scheuble:** Resources, Writing – review & editing. **Magali Cochet:** Conceptualization, Writing – review & editing. **Pierre Boillat:** Funding acquisition, Conceptualization, Writing – review & editing. **Thomas J. Schmidt:** Resources, Project administration, Writing – review & editing. **Felix N. Büchi:**

Funding acquisition, Conceptualization, Writing – review & editing, Supervision.

Declaration of competing interest

The authors declare that they have no known competing financial interests or personal relationships that could have appeared to influence the work reported in this paper.

Data availability

Data will be made available on request.

Acknowledgements

The authors gratefully acknowledge Innosuisse for funding through the Swiss Competence Center for Energy Research: Efficient Technologies and Systems for Mobility (SCCER Mobility). Further, the authors would like to thank Christoph Csoklich and Arnaud Schuller for many discussions on test protocols, Jens Eller for discussions on MEA materials, Zonglan Wei for performing CFD calculations, Roland Gretler for laser-cutting of GDLs, as well as Thomas Gloor and Martin Ammann for technical support (all PSI). Furthermore, the authors acknowledge Abifor AG, Germany for providing samples of hot-melt adhesives.

Appendix A. Supplementary data

Supplementary data to this article can be found online at <https://doi.org/10.1016/j.jpowsour.2022.232419>.

References

- [1] T. Yoshida, K. Kojima, Toyota MIRAI fuel cell vehicle and progress toward a future hydrogen society, *Electrochem. Soc. Interface* 24 (2015) 45, <https://doi.org/10.1149/2.F03152if>.
- [2] W. Sung, Y.-I. Song, K.-H. Yu, T.-W. Lim, Recent advances in the development of Hyundai Kia's fuel cell electric vehicles, *SAE Int J Engines* 3 (2010) 768–772, <https://doi.org/10.4271/2010-01-1089>.
- [3] M. Matsunaga, K. Kimura, T. Fukushima, T. Ogawa, K. Ojima, Fuel cell powertrain for FCX clarity, *Honda RD Tech Rev* 21 (2009) 9.
- [4] Hyundai delivers first XCIENT Fuel Cell trucks to Switzerland, *Fuel Cell. Bull.* 2020 (2020) 3, [https://doi.org/10.1016/S1464-2859\(20\)30328-X](https://doi.org/10.1016/S1464-2859(20)30328-X).
- [5] J. Juriga, Hyundai Motor Group's Development of the Fuel Cell Electric Vehicle, 2020.
- [6] U. Eberle, B. Müller, R. von Helmolt, Fuel cell electric vehicles and hydrogen infrastructure: status 2012, *Energy Environ. Sci.* 5 (2012) 8780–8798, <https://doi.org/10.1039/C2EE22596D>.
- [7] Y. Naganuma, K. Manabe, H. Imanishi, Y. Nonobe, Development of system control for rapid warm-up operation of fuel cell, *SAE Int J Altern Powertrains* 1 (2012) 365–373, <https://doi.org/10.4271/2012-01-1230>.
- [8] B.G. Pollet, I. Staffell, J.L. Shang, Current status of hybrid, battery and fuel cell electric vehicles: from electrochemistry to market prospects, *Electrochim. Acta* 84 (2012) 235–249, <https://doi.org/10.1016/j.electacta.2012.03.172>.
- [9] M. Striednig, S. Brandstätter, M. Sartory, M. Klell, Thermodynamic real gas analysis of a tank filling process, *Int. J. Hydrogen Energy* 39 (2014) 8495–8509, <https://doi.org/10.1016/j.ijhydene.2014.03.028>.
- [10] U.S. Department of Energy, Fuel Cell Technologies Office Multi-Year Research, Development, and Demonstration Plan, 2016.
- [11] A. Kusoglu, A.Z. Weber, New insights into perfluorinated sulfonic-acid ionomers, *Chem. Rev.* 117 (2017) 987–1104, <https://doi.org/10.1021/acs.chemrev.6b00159>.
- [12] A. Wilson, G. Kleen, D. Papageorgopoulos, Fuel Cell System Cost - 2017, DOE Hydrogen and Fuel Cells Program Record, 2017.
- [13] M. Striednig, M. Cochet, P. Boillat, T.J. Schmidt, F.N. Büchi, A model based investigation of evaporative cooling for polymer electrolyte fuel cells – stack level analysis, *J. Power Sources* 517 (2022), 230706, <https://doi.org/10.1016/j.jpowsour.2021.230706>.
- [14] G. Zhang, S.G. Kandlikar, A critical review of cooling techniques in proton exchange membrane fuel cell stacks, *Int. J. Hydrogen Energy* 37 (2012) 2412–2429, <https://doi.org/10.1016/j.ijhydene.2011.11.010>.
- [15] H.R. Kunz, Solid Polymer Electrolyte Fuel Cell System with Porous Plate Evaporative Cooling, 1992. CA1309127C.
- [16] A. Warburton, D. Mossop, B. Burslem, P. Rama, P. Adcock, J. Cole, et al., Development of an Evaporatively Cooled Hydrogen Fuel Cell System and its Vehicle Application, 2013, <https://doi.org/10.4271/2013-01-0475>, 2013-01-0475.
- [17] C.J. Carnevale, T.W. P. Jr., R.M. Darling, P. Badrinarayanan, M.L. Perry, Hybrid Bipolar Plate for Evaporatively Cooled Fuel Cells, US9570763B2, 2017.
- [18] M.L. Perry, J.P. Meyers, R.M. Darling, C. Evans, R. Balliet, Evaporatively-cooled PEM fuel-cell stack and system, *ECS Trans.* 3 (2006) 1207, <https://doi.org/10.1149/1.2356240>.
- [19] T. Scheibert, Verdampfungsgekühltes Brennstoffzellensystem und Verfahren zum Betreiben eines verdampfungsgekühlten Brennstoffzellensystems. EP2225789B1, 2011.
- [20] M. Katz, Fuel Cell Evaporative Cooler, 1993. US5206094A.
- [21] S.G. Goebel, Evaporative Cooled Fuel Cell, US6960404B2, 2005.
- [22] V. Maisotsenko, L.E. Gillan, T.L. Heaton, A.D. Gillan, Fuel Cell Systems with Evaporative Cooling and Methods for Humidifying and Adjusting the Temperature of the Reactant Streams, US6779351B2, 2004.
- [23] J. Stedman, Fuel Cell with Evaporative Cooling, US3761316A, 1973.
- [24] E.J. Choi, S.H. Hwang, J. Park, M.S. Kim, Parametric analysis of simultaneous humidification and cooling for PEMFCs using direct water injection method, *Int. J. Hydrogen Energy* 42 (2017) 12531–12542, <https://doi.org/10.1016/j.ijhydene.2017.03.201>.
- [25] S.H. Hwang, M.S. Kim, An experimental study on the cathode humidification and evaporative cooling of polymer electrolyte membrane fuel cells using direct water injection method at high current densities, *Appl. Therm. Eng.* 99 (2016) 635–644, <https://doi.org/10.1016/j.applthermaleng.2016.01.091>.
- [26] D.L. Wood, J.S. Yi, T.V. Nguyen, Effect of direct liquid water injection and interdigitated flow field on the performance of proton exchange membrane fuel cells, *Electrochim. Acta* 43 (1998) 3795–3809, [https://doi.org/10.1016/S0013-4686\(98\)00139-X](https://doi.org/10.1016/S0013-4686(98)00139-X).
- [27] R. Cohen, Fuel Cell Evaporative Cooling Using Fuel as a Carrier Gas, US4994331A, 1991.
- [28] M. Cochet, A. Forner-Cuenca, V. Manzi, M. Siegwart, D. Scheuble, P. Boillat, Novel concept for evaporative cooling of fuel cells: an experimental study based on neutron imaging, *Fuel Cell.* 18 (2018) 619–626, <https://doi.org/10.1002/fuce.201700232>.
- [29] A. Forner-Cuenca, J. Biesdorf, L. Gubler, P.M. Kristiansen, T.J. Schmidt, P. Boillat, Engineered water highways in fuel cells: radiation grafting of gas diffusion layers, *Adv. Mater.* 27 (2015) 6317–6322, <https://doi.org/10.1002/adma.201503557>.
- [30] A. Forner-Cuenca, V. Manzi-Orezzoli, P.M. Kristiansen, L. Gubler, T.J. Schmidt, P. Boillat, Mask-assisted electron radiation grafting for localized through-volume modification of porous substrates: influence of electron energy on spatial resolution, *Radiat. Phys. Chem.* 135 (2017) 133–141, <https://doi.org/10.1016/j.radphyschem.2017.01.036>.
- [31] A. Forner-Cuenca, J. Biesdorf, A. Lamibrac, V. Manzi-Orezzoli, F.N. Büchi, L. Gubler, et al., Advanced water management in PEFCs: diffusion layers with patterned wettability II. Measurement of capillary pressure characteristic with neutron and synchrotron imaging, *J. Electrochem. Soc.* 163 (2016) F1038–F1048, <https://doi.org/10.1149/2.0511609jes>.
- [32] A. Forner-Cuenca, J. Biesdorf, V. Manzi-Orezzoli, L. Gubler, T.J. Schmidt, P. Boillat, Advanced water management in PEFCs: diffusion layers with patterned wettability III. Operando characterization with neutron imaging, *J. Electrochem. Soc.* 163 (2016) F1389–F1398, <https://doi.org/10.1149/2.0891613jes>.
- [33] A. Forner-Cuenca, V. Manzi-Orezzoli, J. Biesdorf, M.E. Kazzi, D. Streich, L. Gubler, et al., Advanced water management in PEFCs: diffusion layers with patterned wettability I. Synthetic routes, wettability tuning and thermal stability, *J. Electrochem. Soc.* 163 (2016) F788–F801, <https://doi.org/10.1149/2.0271608jes>.
- [34] A. Fly, R.H. Thring, System thermal and water balance in an evaporatively cooled PEM fuel cell vehicle, in: *Veh. Therm. Manag. Syst. Conf. Proc.*, Woodhead Publishing, 2013, pp. 267–277, <https://doi.org/10.1533/9780857094735.6.267>. VTMS11.
- [35] A. Fly, R.H. Thring, Temperature regulation in an evaporatively cooled proton exchange membrane fuel cell stack, *Int. J. Hydrogen Energy* 40 (2015) 11976–11982, <https://doi.org/10.1016/j.ijhydene.2015.04.086>.
- [36] A. Fly, R.H. Thring, A comparison of evaporative and liquid cooling methods for fuel cell vehicles, *Int. J. Hydrogen Energy* 41 (2016) 14217–14229, <https://doi.org/10.1016/j.ijhydene.2016.06.089>.
- [37] M. Schultze, J. Horn, A control oriented simulation model of an evaporation cooled polymer electrolyte membrane fuel cell system, *IFAC Proc* 44 (2011) 14790–14795, <https://doi.org/10.3182/20110828-6-IT-1002.00311>.
- [38] A.Z. Weber, R.M. Darling, Understanding porous water-transport plates in polymer-electrolyte fuel cells, *J. Power Sources* 168 (2007) 191–199, <https://doi.org/10.1016/j.jpowsour.2007.02.078>.
- [39] M. Striednig, T.J. Schmidt, F.N. Büchi, A model based investigation of evaporative cooling for polymer electrolyte fuel cells – system level analysis, *J. Power Sources* 542 (2022), 231720, <https://doi.org/10.1016/j.jpowsour.2022.231720>.
- [40] J. Dujc, A. Forner-Cuenca, P. Marmet, M. Cochet, R. Vetter, J.O. Schumacher, et al., Modeling the effects of using gas diffusion layers with patterned wettability for advanced water management in proton exchange membrane fuel cells, *J. Electrochem. Energy Convers. Storage* 15 (2018), 021001, <https://doi.org/10.1115/1.4038626>. –021001.
- [41] M.A. Safi, J. Mantzaras, N.I. Prasianakis, A. Lamibrac, F.N. Büchi, A pore-level direct numerical investigation of water evaporation characteristics under air and hydrogen in the gas diffusion layers of polymer electrolyte fuel cells, *Int. J. Heat Mass Tran.* 129 (2019) 1250–1262, <https://doi.org/10.1016/j.ijheatmasstransfer.2018.10.042>.
- [42] M.A. Safi, N.I. Prasianakis, J. Mantzaras, A. Lamibrac, F.N. Büchi, Experimental and pore-level numerical investigation of water evaporation in gas diffusion layers

- of polymer electrolyte fuel cells, *Int. J. Heat Mass Tran.* 115 (2017) 238–249, <https://doi.org/10.1016/j.ijheatmasstransfer.2017.07.050>.
- [43] L. Capone, P. Marmet, L. Holzer, J. Dujc, J.O. Schumacher, A. Lamibrac, et al., An ensemble Monte Carlo simulation study of water distribution in porous gas diffusion layers for proton exchange membrane fuel cells, *J Electrochem Energy Convers Storage* 15 (2018), <https://doi.org/10.1115/1.4038627>, 031005–031005–10.
- [44] S. Lal, A. Lamibrac, J. Eller, F.N. Büchi, Determination of water evaporation rates in gas diffusion layers of fuel cells, *J. Electrochem. Soc.* 165 (2018) F652–F661, <https://doi.org/10.1149/2.0831809jes>.
- [45] I.V. Zenyuk, A. Lamibrac, J. Eller, D.Y. Parkinson, F. Marone, F.N. Büchi, et al., Investigating evaporation in gas diffusion layers for fuel cells with X-ray computed tomography, *J. Phys. Chem. C* 120 (2016) 28701–28711, <https://doi.org/10.1021/acs.jpcc.6b10658>.
- [46] A. Mularczyk, A. Michalski, M. Striednig, R. Herrendörfer, T.J. Schmidt, F. N. Büchi, et al., Mass transport limitations of water evaporation in polymer electrolyte fuel cell gas diffusion layers, *Energies* 14 (2021) 2967, <https://doi.org/10.3390/en14102967>.
- [47] M. Cochet, A. Forner-Cuenca, V. Manzi-Orezzoli, M. Siegwart, D. Scheuble, P. Boillat, Enabling high power density fuel cells by evaporative cooling with advanced porous media, *J. Electrochem. Soc.* 167 (2020), 084518, <https://doi.org/10.1149/1945-7111/ab8e82>.
- [48] C. Simon, F. Hasche, H.A. Gasteiger, Influence of the gas diffusion layer compression on the oxygen transport in PEM fuel cells at high water saturation, *Levels* 164 (2017), <https://doi.org/10.1149/2.0691706jes>.
- [49] *Evaluation of measurement data - guide to the expression of uncertainty in measurement*, in: Document Produced by Working Group 1 of the Joint Committee for Guides in Metrology, JCGM/WG 1), 2008.
- [50] M. Grimm, M. Hellmann, H. Kemmer, S. Kabelac, Water management of PEM fuel cell systems based on the humidity distribution in the anode gas channels, *Fuel Cell*. 20 (2020) 477–486, <https://doi.org/10.1002/fuce.202000070>.
- [51] W. Gu, D.R. Baker, Y. Liu, H.A. Gasteiger, Proton exchange membrane fuel cell (PEMFC) down-the-channel performance model, in: *Handb. Fuel Cells*, John Wiley & Sons, Ltd, 2003.